

Six Degree-of-Freedom Hovering using LIDAR Altimetry via Reinforcement Meta-Learning

Brian Gaudet*

DeepAnalytX LLC, Bishop CA 93514

Richard Linares†

Massachusetts Institute of Technology, Cambridge, MA 02139

Robert Furfaro‡

University of Arizona, 1127 E. Roger Way, Tucson Arizona, 85721

We optimize a six degrees of freedom hovering policy using reinforcement meta-learning. The policy maps flash LIDAR measurements directly to on/off spacecraft body-frame thrust commands, allowing hovering at a fixed position and attitude in the asteroid body-fixed reference frame. Importantly, the policy does not require position and velocity estimates, and can operate in environments with unknown dynamics, and without an asteroid shape model or navigation aids. Indeed, during optimization the agent is confronted with a new randomly generated asteroid for each episode, insuring that it does not learn an asteroid’s shape, texture, or environmental dynamics. This allows the deployed policy to generalize well to novel asteroid characteristics, which we demonstrate in our experiments. The hovering controller has the potential to simplify mission planning by allowing asteroid body-fixed hovering immediately upon the spacecraft’s arrival to an asteroid. This in turn simplifies shape model generation and allows resource mapping via remote sensing immediately upon arrival at the target asteroid.

I. Introduction

RECENTLY there has been increased interest in robotic missions to near Earth asteroids, for both scientific and commercial purposes. The prevalent concept of operations requires complete characterization of the asteroid’s shape and dynamics prior to a sample return maneuver. Before a shape model can even be generated, the environmental dynamics must be characterized to a high degree of accuracy in order to allow calculation of stable orbits from which shape model generation takes place [1]. Moreover, these stable orbits are in general only possible over a limited range of latitudes [2]. Asteroid body-fixed hovering at arbitrary locations in proximity to the asteroid has the potential to simplify mission planning, allowing high resolution sensor measurements at arbitrary locations [3]. Hovering in the inertial frame with the asteroid rotating below the spacecraft is possible at arbitrary altitudes (within the limits of terrain hazards) and in general will require less fuel than hovering in the asteroid body-fixed frame. Although hovering in the asteroid body-fixed frame requires more fuel expenditure and cannot be performed at large distances from the asteroid, body frame hovering has the advantage of allowing multiple sensor measurements from a fixed position with respect to the asteroid. Moreover, body fixed hovering close to the surface would allow a spacecraft to drill or collect surface samples while compensating for the force induced by the manipulators. Clearly, both types of hovering would be useful for asteroid missions.

Previous work in hovering in close proximity to asteroids includes [4], where the authors develop a hovering controller that uses altimetry measurements to hover in the asteroid body-fixed frame. This work uses a single altimeter and thrusting direction, but assumes the sensor is aligned with the gravitational acceleration at the hovering point, the altitude is below the resonance radius (the altitude where gravitational and centrifugal forces cancel), and that the centrifugal force components perpendicular to thrust direction are known. Furfaro develops a 3-DOF hovering controller using sliding mode control theory, but assumes that a navigation system can infer the spacecraft’s position and velocity in the asteroid centered reference frame, which in general is not possible without a preexisting shape model[5]. Using a shape model, Gaudet and Furfaro demonstrate both hovering and TAG maneuvers using a particle filter to infer the

*Co-founder, briangaudet@mac.com

†Charles Stark Draper Assistant Professor, Department of Aeronautics and Astronautics

‡Professor, Department of Systems and Industrial Engineering, Department of Aerospace and Mechanical Engineering

spacecraft's position and velocity[6]. Lee et. al. demonstrates 6-DOF hovering using a control law developed in the Lie group SE(3)[7], but again assumes the spacecraft's state can be inferred, and requires an estimate of the environmental dynamics. Gaudet and Furfaro developed a 3-DOF hovering controller using reinforcement learning[8] and showed improved transient response as compared to an LQR controller; however, the method assumes that the spacecraft's position and velocity can be inferred. None of this work treats the case where the spacecraft arrives at an asteroid and we want the spacecraft to be able to immediately hover in the body-fixed frame when both 1.) there is no knowledge of the environmental dynamics and 2.) there is not an existing shape model that can be used by a navigation system to infer the spacecraft's position and velocity.

In this work we focus on the body-fixed hovering problem, where the spacecraft can be commanded to hover at its current position and attitude. By body-fixed, we mean that the spacecraft's position remains fixed with respect to the asteroid's surface. In contrast, when hovering in the asteroid centered inertial reference frame the asteroid rotates below the spacecraft. Unlike previous work, we do not assume that the spacecraft can infer position and velocity from measurements (as is possible with a preexisting shape model) and that the environmental dynamics are unknown (except to the extent required for thruster sizing). The goal is to remain at a constant asteroid body-fixed position and attitude from the commencement of the hovering maneuver. We will assume that the spacecraft is equipped with a flash LIDAR system, gyroscopes that can measure the change in the spacecraft's attitude from the initiation of the hovering maneuver, and rate gyros that measure rotational velocity. We further assume that these sensors can provide measurements every 6s. At the start of the hovering maneuver, the spacecraft is pointed in the general direction of the asteroid, and consequently at least some of the flash LIDAR elements can return valid altimeter readings.

Our hovering controller is optimized using reinforcement learning (RL), which learns a policy that maps sensor measurements directly to on/off thrust commands, and that can adapt to unknown environmental dynamics. Adaptability is achieved through RL-Meta Learning [9–11], where different environmental dynamics, are treated as a range of partially observable Markov decision processes (POMDP). In each POMDP, the policy's recurrent network hidden state will evolve differently over the course of an episode, capturing information about hidden variables such as external forces and changes in the spacecraft's internal dynamics that are used to minimize the cost function. By optimizing the policy over this range of POMDPs, the trained policy will be able to adapt to novel POMDPs encountered during deployment. Specifically, even though the policy's parameters are fixed after optimization, the policy's hidden state will evolve based off the current POMDP, thus adapting to the environment. We have demonstrated the effectiveness of RL meta-learning to create adaptive policies for aerospace applications in previous work [12–14]. In this work, each randomly generated asteroid is a new POMDP. Through Meta-RL optimization, the agent learns a policy that allows it to hover effectively in the body-fixed frame of asteroid's with novel shape, dynamics, and texture. Our goal is for the policy to hover at a position within 2m of the initial position with fuel expenditure minimized during hovering. Importantly, the optimized policy will be general in that it will allow hovering over *any* asteroid with arbitrary shape, rotation, and density, within the limits of thruster capability. To achieve this, the agent learns the policy in an environment that generates a new random asteroid for each episode.

The optimized policy serves as an integrated guidance, navigation, and control system for the purposes of a hovering maneuver, and interfaces with peripheral spacecraft systems as shown below in Fig. 1.

II. Problem Formulation

A. Spacecraft Configuration

The spacecraft is modeled as a uniform density cube with height $h = 2$, width $w = 2$, and depth $d = 2$, with inertia matrix given in Eq. (1). The spacecraft has a wet mass ranging from 450 to 500 kg. The thruster configuration is shown in Table 1, where x , y , and z are the body frame axes. Roll is about the x -axis, yaw is about the z -axis, and pitch is about the y -axis. Firing both thrusters on a face give translational thrust without rotation, while firing a single thruster on a given face induces a torque. The navigation system provides updates to the guidance system every 6 s, and we integrate the equations of motion using fourth order Runge-Kutta integration with a time step of 2 s.

$$\mathbf{J} = \frac{m}{12} \begin{bmatrix} h^2 + d^2 & 0 & 0 \\ 0 & w^2 + d^2 & 0 \\ 0 & 0 & w^2 + h^2 \end{bmatrix} \quad (1)$$

m is the spacecraft's mass, which is updated as shown in Eq. (6c).

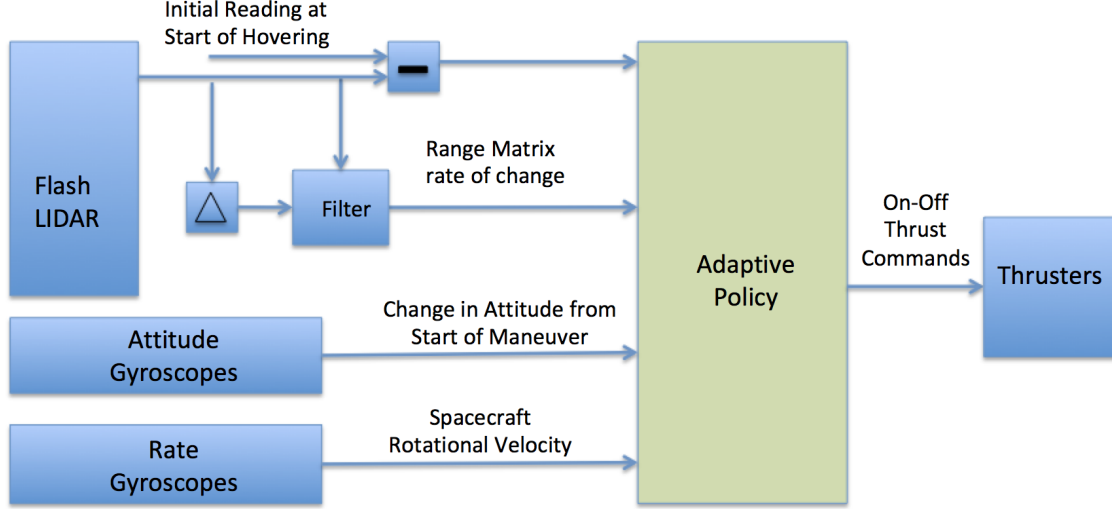


Fig. 1 Deployed Policy Interface with Peripheral Systems

Table 1 Body Frame Thruster Locations.

Thruster	x (m)	y (m)	z (m)	Thrust
1	-1.0	0.0	0.8	1.0
2	-1.0	0.0	-0.8	1.0
3	1.0	0.0	0.8	1.0
4	1.0	0.0	-0.8	1.0
5	-0.8	-1.0	0.0	1.0
6	0.8	-1.0	0.0	1.0
7	-0.8	1.0	0.0	1.0
8	0.8	1.0	0.0	1.0
9	0.0	-0.8	-1.0	1.0
10	0.0	0.8	-1.0	1.0
11	0.0	-0.8	1.0	1.0
12	0.0	0.8	1.0	1.0

B. Asteroid and Sensor Models

Since our goal is for the agent to hover about an asteroid with unknown shape, we need to insure that the agent does not learn the asteroid's shape during optimization. To this end, we randomly generate a new asteroid for each episode. Each asteroid starts as an icosahedron, after which we recursively (twice) expand each face into four equal triangles, with the new vertices projected onto the sphere. We then randomly generate the asteroid's a , b , and c axes over the range (400, 300, 200) to (600, 500, 400) meters, and we scale the vertices appropriately. Each vertex is then perturbed uniformly over a range from 0 to 5%. A sample randomly generated asteroid with 1280 faces and 642 vertices is shown below in Fig. 2.

For the modeling of environmental dynamics, we model the asteroid as an ellipsoid with uniform density. We assume that the asteroid is in general not rotating about a principal axis, and therefore to calculate the angular velocity vector we must specify the spin rate, the nutation angle (angle between the asteroid's z -axis and the axis of rotation), and moments of inertia [15]. The moments of inertia in turn depend on the asteroid's density and dimensions. The dimensions are specified by the ellipsoid axes $a > b == c$, where assuming $b == c$ significantly simplifies the equations of motion. Since for the random asteroid the b and c axes are not in general equal, we average them for purposes of calculating the asteroid's rotational velocity components. We use a gravity model that assumes a uniformly distributed ellipsoid[15].

The flash LIDAR is modeled as an 8 X 8 array of range sensors. Current commercial flash LIDAR units typically have a 100 X 100 sensor array, but the smaller sensor array allows much faster computation during optimization, and it

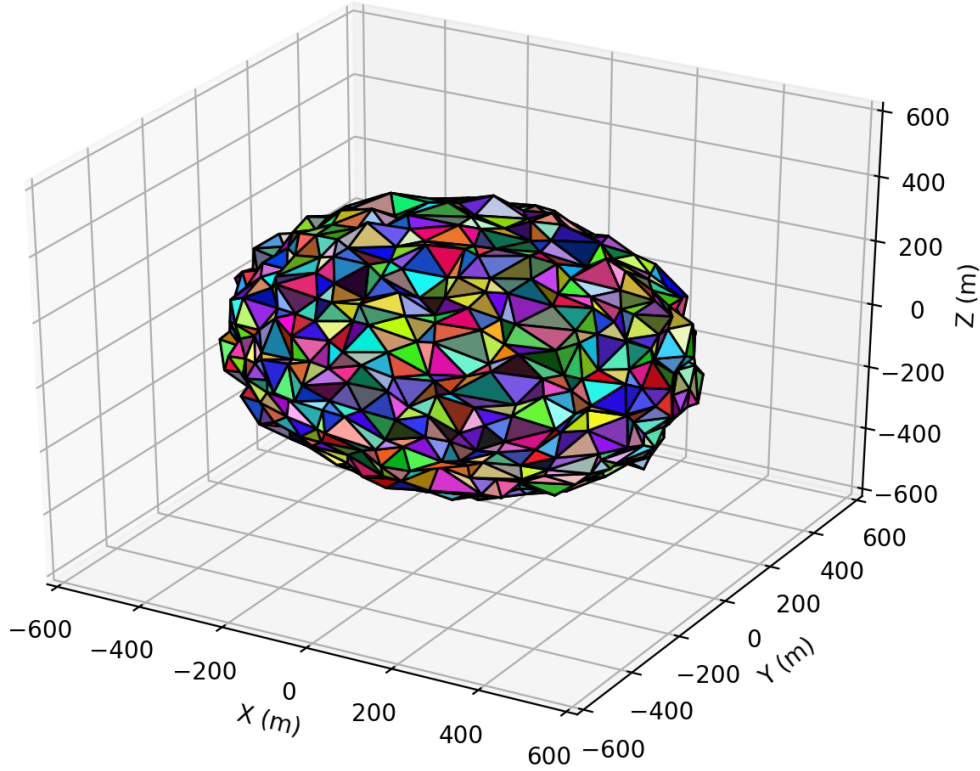


Fig. 2 Sample Random Asteroid

seems intuitive that if hovering performance is satisfactory with an 8 X 8 array, it would likely be even better with a 100 X 100 array. We use the Moller-Trumbore ray casting algorithm[16] to compute the intersection of each LIDAR beam with a triangle in the randomly generated asteroid. Our implementation only returns a range if a triangle is intersected on the correct side, and the intersection point is not occluded by another triangle. If a beam fails to intersect a triangle, a max range reading of 2000m is returned.

We also assume the spacecraft is equipped with a gyroscope that can measure the spacecraft's change in attitude (measured from the initiation of hovering), and a rate gyroscope to measure rotational velocity.

C. Equations of Motion

The force \mathbf{F}_B and torque \mathbf{L}_B in the lander's body frame for a given commanded thrust depends on the placement of the thrusters in the lander structure. We can describe the placement of each thruster through a body-frame direction vector \mathbf{d} and position vector \mathbf{r} , both in \mathbb{R}^3 . The direction vector is a unit vector giving the direction of the body frame force that results when the thruster is fired. The position vector gives the body frame location with respect to the center of mass, where the force resulting from the thruster firing is applied for purposes of computing torque, and in general the center of mass varies with time as fuel is consumed. For a lander with k thrusters, the body frame force and torque associated with one or more thrusters firing is then as shown in Equations (2a) and (2b), where $T_{cmd_i} \in [T_{min}, T_{max}]$ is the commanded thrust for thruster i , T_{min} and T_{max} are a thruster's minimum and maximum thrust, $\mathbf{d}^{(i)}$ the direction vector for thruster i , and $\mathbf{r}^{(i)}$ the position of thruster i . The total body frame force and torque are calculated by summing

Table 2 Parameters for Randomly Generated Asteroids

Parameter	min	max
a-axis (m)	400	600
b-axis (m)	300	500
c-axis (m)	200	400
Density ρ g/cm ³	0.5	5
Spin Rate ω_o (rad/s)	5×10^{-4}	1×10^{-6}
Nutation Angle (degrees)	60	90
Acceleration due to SRP m/s ²	$[-100, -100, -100] \times 10^{-6}$	$[100, 100, 100] \times 10^{-6}$

the individual forces and torques.

$$\mathbf{F}_B = \sum_{i=1}^k \mathbf{d}^{(i)} T_{cmd}^{(i)} \quad (2a)$$

$$\mathbf{L}_B = \sum_{i=1}^k (\mathbf{r}^{(i)} - \mathbf{r}_{com}) \times \mathbf{F}_B^{(i)} \quad (2b)$$

The dynamics model uses the lander's current attitude \mathbf{q} to convert the body frame thrust vector to the inertial frame as shown in in Equation (3) where $[\mathbf{BN}](\mathbf{q})$ is the direction cosine matrix mapping the inertial frame to body frame obtained from the current attitude parameter \mathbf{q} .

$$\mathbf{F}_N = [[\mathbf{BN}](\mathbf{q})]^T \mathbf{F}_B \quad (3)$$

The rotational velocities $\omega_{B/N}$ are then obtained by integrating the Euler rotational equations of motion, as shown in Equation (4), where \mathbf{L}_B is the body frame torque as given in Equation (2b), \mathbf{L}_{env} is the body frame torque from external disturbances, and \mathbf{J} is the lander's inertia tensor. Note we have included a term that models a rotation induced by a changing inertia tensor.

$$\mathbf{J}\dot{\omega}_B = -\tilde{\omega}_B \mathbf{J} \omega_B - \mathbf{J} \omega + \mathbf{L}_B + \mathbf{L}_{B_{env}} \quad (4)$$

The lander's attitude is then updated by integrating the differential kinematic equations shown in Equation (5), where the lander's attitude is parameterized using the quaternion representation and ω_i denotes the i^{th} component of the rotational velocity vector ω_B .

$$\begin{bmatrix} \dot{q}_0 \\ \dot{q}_1 \\ \dot{q}_2 \\ \dot{q}_3 \end{bmatrix} = \frac{1}{2} \begin{bmatrix} q_0 & -q_1 & -q_2 & -q_3 \\ q_1 & q_0 & -q_3 & q_2 \\ q_2 & q_3 & q_0 & -q_1 \\ q_3 & -q_2 & q_1 & q_0 \end{bmatrix} \begin{bmatrix} 0 \\ \omega_0 \\ \omega_1 \\ \omega_2 \end{bmatrix} \quad (5)$$

The translational motion is modeled as shown in 6a through 6c.

$$\dot{\mathbf{r}} = \mathbf{v} \quad (6a)$$

$$\dot{\mathbf{v}} = \frac{\mathbf{F}_N}{m} + \mathbf{a}_{env} - g(\mathbf{r}, a, b, c, \rho) + 2\mathbf{r} \times \omega_a + (\omega_a \times \mathbf{r}) \times \omega_a \quad (6b)$$

$$\dot{m} = -\frac{\sum_i^k \|\mathbf{F}_B^{(i)}\|}{I_{sp} g_{ref}} \quad (6c)$$

Here $\mathbf{F}_N^{(i)}$ is the inertial frame force as given in Eq. (3), k is the number of thrusters, $g_{ref} = 9.8 \text{ m/s}^2$, \mathbf{r} is the spacecraft's position in the asteroid centered reference frame, $g(\mathbf{r}, a, b, c, \rho)$ is an ellipsoid gravity model as described in Reference(15), ρ is the asteroid's density, a, b, c are the asteroid's semi-axis lengths in meters, $I_{sp} = 225 \text{ s}$, and the

spacecraft's mass is m . \mathbf{a}_{env} is a vector representing solar radiation pressure. ω_a is the asteroid's rotational velocity vector, which we compute as shown in Equations (7a) through (7f), which uses the simplifying assumption that $J_x = J_y$ [4]. Here ω_o is the asteroid's spin rate and θ the nutation angle between the asteroid's spin axis and z-axis. We modified the equations from Reference (4) to add the phase term ϕ to handle the case where the spacecraft starts the maneuver at an arbitrary point in the asteroid's rotational cycle.

$$\omega_{a_x} = \omega_o \sin \theta \cos (\omega_n t + \phi) \quad (7a)$$

$$\omega_{a_y} = \omega_o \sin \theta \sin (\omega_n t + \phi) \quad (7b)$$

$$\omega_{a_z} = \omega_o \cos \theta \quad (7c)$$

$$\omega_n = \sigma \omega_o \cos \theta \quad (7d)$$

$$J_{x,y}/J_z = (b^2 + c^2)/(a^2 + b^2) \quad (7e)$$

$$\sigma = \frac{(J_z - J_x)}{J_x} \quad (7f)$$

III. Guidance Law Development

A. RL Overview

In the RL framework, an agent learns through episodic interaction with an environment how to successfully complete a task by learning a policy that maps observations to actions. The environment initializes an episode by randomly generating a ground truth state, mapping this state to an observation, and passing the observation to the agent. These observations could be a corrupted version of the ground truth state (to model sensor noise) or could be raw sensor outputs such as Doppler radar altimeter readings, a multi-channel pixel map from an electro-optical sensor, or in our case, a flash LIDAR range matrix. The agent uses this observation to generate an action that is sent to the environment; the environment then uses the action and the current ground truth state to generate the next state and a scalar reward signal. The reward and the observation corresponding to the next state are then passed to the agent. The process repeats until the environment terminates the episode, with the termination signaled to the agent via a done signal. Possible termination conditions include the agent completing the task, satisfying some condition on the ground truth state (such as altitude falling below zero), or violating a constraint.

A Markov Decision Process (MDP) is an abstraction of the environment, which in a continuous state and action space, can be represented by a state space \mathcal{S} , an action space \mathcal{A} , a state transition distribution $\mathcal{P}(\mathbf{x}_{t+1}|\mathbf{x}_t, \mathbf{u}_t)$, and a reward function $r = \mathcal{R}(\mathbf{x}_t, \mathbf{u}_t)$, where $\mathbf{x} \in \mathcal{S}$ and $\mathbf{u} \in \mathcal{A}$, and r is a scalar reward signal. We can also define a partially observable MDP (POMDP), where the state \mathbf{x} becomes a hidden state, generating an observation \mathbf{o} using an observation function $\mathcal{O}(\mathbf{x})$ that maps states to observations. The POMDP formulation is useful when the observation consists of raw sensor outputs, as is the case in this work. In the following, we will refer to both fully observable and partially observable environments as POMDPs, as an MDP can be considered a POMDP with an identity function mapping states to observations.

The agent operates within an environment defined by the POMDP, generating some action \mathbf{u}_t based off of the observation \mathbf{o}_t , and receiving reward r_{t+1} and next observation \mathbf{o}_{t+1} . Optimization involves maximizing the sum of (potentially discounted) rewards over the trajectories induced by the interaction between the agent and environment. Constraints such as minimum and maximum thrust, glide slope, attitude compatible with sensor field of view, maximum rotational velocity, and terrain feature avoidance (such as targeting the bottom of a deep crater) can be included in the reward function, and will be accounted for when the policy is optimized. Note that there is no guarantee on the optimality of trajectories induced by the policy, although in practice it is possible to get close to optimal performance by tuning the reward function.

Reinforcement meta-learning differs from generic reinforcement learning in that the agent learns to quickly adapt to novel POMDPs by learning over a wide range of POMDPs. These POMDPs can include different environmental dynamics, actuator failure scenarios, mass and inertia tensor variation, and varying amounts of sensor distortion. Learning within the RL meta-learning framework results in an agent that can quickly adapt to novel POMDPs, often with just a few steps of interaction with the environment. There are multiple approaches to implementing meta-RL. In Reference (17), the authors design the objective function to explicitly make the model parameters transfer well to new tasks. In Reference (9), the authors demonstrate state of the art performance using temporal convolutions with soft

attention. And in Reference (10), the authors use a hierarchy of policies to achieve meta-RL. In this proposal, we use a different approach[11] using a recurrent policy and value function. Note that it is possible to train over a wide range of POMDPs using a non-meta RL algorithm[18]. Although such an approach typically results in a robust policy, the policy cannot adapt in real time to novel environments.

In this work, we implement metal-RL using proximal policy optimization (PPO) [19] with both the policy and value function implementing recurrent layers in their networks. To understand how recurrent layers result in an adaptive agent, consider that given some ground truth agent position, velocity, attitude, and rotational velocity \mathbf{x}_t , and action vector \mathbf{u}_t output by the agent's policy, the next state \mathbf{x}_{t+1} and observation \mathbf{o}_{t+1} depends not only on \mathbf{x}_t and \mathbf{u}_t , but also on the ground truth agent mass, inertia tensor, and external forces acting on the agent. Consequently, during training, the hidden state of a network's recurrent network evolves differently depending on the observed sequence of observations from the environment and actions output by the policy. Specifically, the trained policy's hidden state captures unobserved (potentially time-varying) information such as external forces that are useful in minimizing the cost function. In contrast, a non-recurrent policy (which we will refer to as an MLP policy), which does not maintain a persistent hidden state vector, can only optimize using a set of current observations, actions, and advantages, and will tend to under-perform a recurrent policy on tasks with randomized dynamics, although as we have shown in (Reference 18), training with parameter uncertainty can give good results using an MLP policy, provided the parameter uncertainty is not too extreme. After training, although the recurrent policy's network weights are frozen, the hidden state will continue to evolve in response to a sequence of observations and actions, thus making the policy adaptive. In contrast, an MLP policy's behavior is fixed by the network parameters at test time.

The PPO algorithm used in this work is a policy gradient algorithm which has demonstrated state-of-the-art performance for many RL benchmark problems. PPO approximates the TRPO optimization process[20] by accounting for the policy adjustment constraint with a clipped objective function. The objective function used with PPO can be expressed in terms of the probability ratio $p_k(\theta)$ given by Eq. (8), where π_θ is the policy parameterized by parameter vector θ .

$$p_k(\theta) = \frac{\pi_\theta(\mathbf{u}_k | \mathbf{o}_k)}{\pi_{\theta_{\text{old}}}(\mathbf{u}_k | \mathbf{o}_k)} \quad (8)$$

The PPO objective function is then given in Eq. (9):

$$J(\theta) = \mathbb{E}_{p(\tau)} [\min [p_k(\theta), \text{clip}(p_k(\theta), 1 - \epsilon, 1 + \epsilon)] A_{\mathbf{w}}^\pi(\mathbf{o}_k, \mathbf{u}_k)] \quad (9)$$

This clipped objective function has been shown to maintain a bounded KL divergence with respect to the policy distributions between updates, which aids convergence by insuring that the policy does not change drastically between updates. Our implementation of PPO uses an approximation to the advantage function that is the difference between the empirical return and a state value function baseline, as shown in Equation 10:

$$A_{\mathbf{w}}^\pi(\mathbf{x}_k, \mathbf{u}_k) = \left[\sum_{\ell=k}^T \gamma^{\ell-k} r(\mathbf{o}_\ell, \mathbf{u}_\ell) \right] - V_{\mathbf{w}}^\pi(\mathbf{x}_k) \quad (10)$$

Here the value function $V_{\mathbf{w}}^\pi$ parameterized by vector \mathbf{w} is learned using the cost function given by Eq. (11), where γ is a discount rate applied to rewards generated by reward function $\mathcal{R}(\mathbf{o}, \mathbf{u})$. The discounting of rewards improves optimization performance by improving temporal credit assignment.

$$L(\mathbf{w}) = \sum_{i=1}^M \left(V_{\mathbf{w}}^\pi(\mathbf{o}_k^i) - \left[\sum_{\ell=k}^T \gamma^{\ell-k} \mathcal{R}(\mathbf{u}_\ell^i, \mathbf{o}_\ell^i) \right] \right)^2 \quad (11)$$

In practice, policy gradient algorithms update the policy using a batch of trajectories (roll-outs) collected by interaction with the environment. Each trajectory is associated with a single episode, with a sample from a trajectory collected at step k consisting of observation \mathbf{o}_k , action \mathbf{u}_k , and reward $r_k = \mathcal{R}(\mathbf{o}_k, \mathbf{u}_k)$. Finally, gradient ascent is performed on θ and gradient decent on \mathbf{w} and update equations are given by

$$\mathbf{w}^+ = \mathbf{w}^- - \beta_{\mathbf{w}} \nabla_{\mathbf{w}} L(\mathbf{w})|_{\mathbf{w}=\mathbf{w}^-} \quad (12)$$

$$\theta^+ = \theta^- + \beta_{\theta} \nabla_{\theta} J(\theta)|_{\theta=\theta^-} \quad (13)$$

where $\beta_{\mathbf{w}}$ and β_{θ} are the learning rates for the value function, $V_{\mathbf{w}}^\pi(\mathbf{o}_k)$, and policy, $\pi_{\theta}(\mathbf{u}_k | \mathbf{o}_k)$, respectively.

In our implementation, we dynamically adjust the clipping parameter ϵ to target a KL divergence between policy updates of 0.001. The policy and value function are learned concurrently, as the estimated value of a state is policy dependent. The policy uses a Multi-categorical policy distribution, where a separate observation conditional categorical distribution is maintained for each element of the action vector. Note that exploration in this case is conditioned on the observation, with the two logits associated with each element of the action vector determining how peaked the softmax distribution becomes for each action. Because the log probabilities are calculated using the logits, the degree of exploration automatically adapts during learning such that the objective function is maximized. Finally, note that a full categorical distribution would be impractical, as the number of labels would be 2^{12} , as opposed to 2×12 for the multi-categorical distribution.

B. Guidance Law Optimization

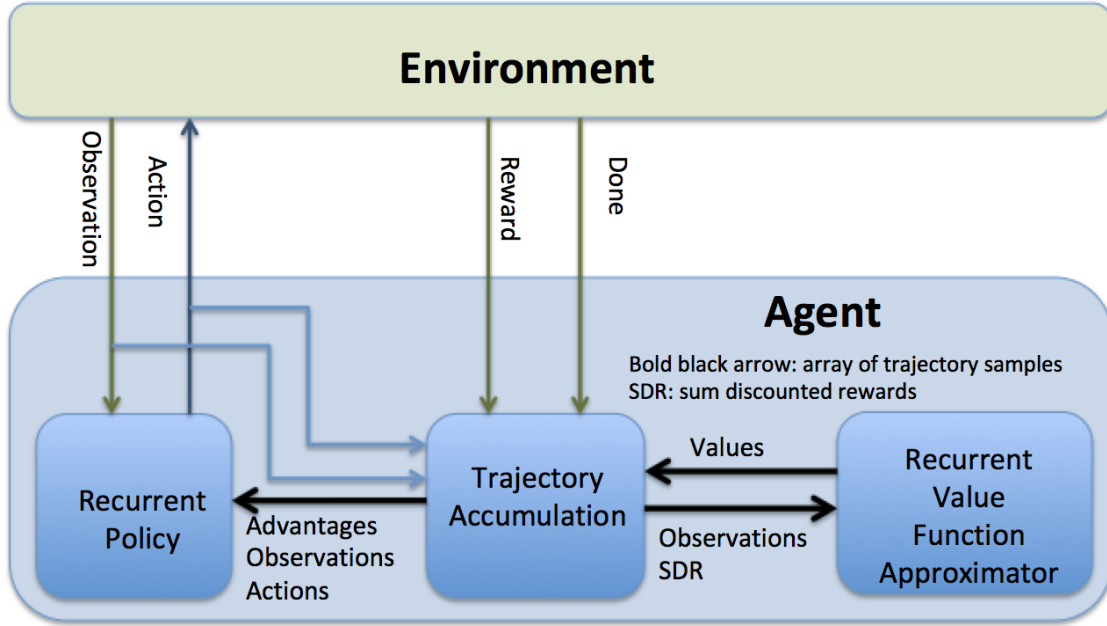


Fig. 3 Agent-Environment Interface

A simplified view of the agent and environment are shown in Figure 3. The environment instantiates the system dynamics model, asteroid shape model, reward function, spacecraft model, and thruster model. Note that when using a policy gradient method such as PPO it suffices to deploy the policy, and it is not necessary to deploy the value function. We can take advantage of this by giving the value function access to the ground truth state during optimization, whereas the policy only has access to the observations, in this case the flash LIDAR measurements. Specifically, the value function has access to the observation given in Eq. (14), where \mathbf{r}_{err} and $d\mathbf{q}$ are the changes in the agent's position and attitude since the initiation of the hovering maneuver, \mathbf{v} is the agent's velocity, and $\boldsymbol{\omega}$ the spacecraft's rotational velocity.

$$\text{obs}_{\text{VF}} = \begin{bmatrix} \mathbf{r}_{\text{err}} & \mathbf{v} & d\mathbf{q} & \boldsymbol{\omega} \end{bmatrix} \quad (14)$$

On the other hand, the policy only has access to the difference between the matrix of flash LIDAR readings at the current timestep and the readings at the start of the hovering maneuver \mathbf{R}_{err} , the change in LIDAR readings between consecutive measurements $d\mathbf{R}$, along with the estimated rotational velocity $\boldsymbol{\omega}$ and change in attitude since the start of the hovering maneuver $d\mathbf{q}$. Using \mathbf{R}_{err} as opposed to the actual range matrix \mathbf{R} allows the agent to generalize better to different altitude ranges. Note that in an actual implementation, $d\mathbf{R}$ would be smoothed with a Kalman filter. The observation given to the policy is then as shown in Eq. (15).

$$\text{obs}_{\pi} = \begin{bmatrix} \mathbf{R}_{\text{err}} & d\mathbf{R} & d\mathbf{q} & \boldsymbol{\omega} \end{bmatrix} \quad (15)$$

The action space is in \mathbb{Z}^k , where k is the number of thrusters. Each element of the agent action $\mathbf{u} \in 0, 1$ is used to index Table 1, where if the action is 1, it is used to compute the body frame force and torque contributed by that thruster.

The value function is implemented using a four layer neural network with tanh activations on each hidden layer. Layer 2 for the value function network is a recurrent layer implemented as a gated recurrent unit [21]. The network architecture is as shown in Table 3, where n_{hi} is the number of units in layer i and obs_dim is the observation dimension

Table 3 Value Function network architecture

Layer	# units	activation
hidden 1	$10 * \text{obs_dim}$	tanh
hidden 2	$\sqrt{n_{h1} * n_{h3}}$	tanh
hidden 3	5	tanh
output	1	linear

The policy has a convolutional front end with an architecture inspired by [22], where the pooling layer is replaced by a 2-D convolutional layer with stride 2. We have found that this improves performance for RL applications. We use rectified linear activations units for each convolutional layer. The first convolutional layer has 2 channels (one for the range readings, the other for the difference in range readings), 8 filters, a filter size of 3, and stride of 1. The second convolutional layer has 8 channels and 8 filters, a filter size of 4, and a stride of 2. The final layers are fully connected, as shown in 4. The entire policy network is diagrammed in Fig. 4. The policy and value functions are periodically updated during optimization after accumulating trajectory rollouts of 30 simulated episodes.

Table 4 Fully Connected Policy network layers

Layer	# units	activation
FC 1	70	tanh
FC 2	154	tanh
FC 3	120	tanh
FC 4	12	linear

During optimization, the agent is given negative rewards proportional to the cumulative change in position from the start of the hovering maneuver. Large negative rewards are given for exceeding a maximum rotational velocity of 0.10 rad/s or if the attitude is such that all of the flash LIDAR elements miss the asteroid, which is detected by all elements returning a max range reading of 2000m. Constraint violation also results in the termination of the current episode. Small negative rewards are given proportional to the control effort at each timestep.

Finally, we provide a terminal reward bonus when the spacecraft executes a good landing (see below). The reward function is then given by Equation (16), where the various terms are described in the following:

- 1) α weights a term penalizing the current deviation from desired hovering position.
- 2) β weights a term penalizing deviation from desired hovering attitude.
- 3) γ weights a term penalizing control effort.
- 4) η is a constant positive term that encourages the agent to keep making progress along the trajectory.
- 5) ζ is a bonus given for satisfying a terminal constraint at the end of the hovering maneuver, where the spacecraft's terminal position and velocity are all within specified limits. The limits are $\|\mathbf{r}\| = 2$ m, $\|\mathbf{v}\| = 0.1$, m/s, and all components of angular velocity less than 0.025 rad/sec
- 6) κ is a penalty for exceeding any constraint. We impose a rotational velocity constraint of 0.10 rad/sec for all three rotational axes. We also constrain the spacecraft's attitude such that at least one LIDAR beam hits the asteroid.

$$r = \alpha r_{err} + \beta q_{error} + \gamma \|\mathbf{T}\| + \eta + \zeta(\text{terminal constraints satisfied}) + \kappa(\text{constraint violation}) \quad (16)$$

Initial hyperparameter settings are shown in Table 5.

IV. Experiments

The spacecraft initial condition limits for these experiments were selected assuming that the spacecraft would start with its sensor pointed in the general direction of the asteroid with minimal residual translational and rotational velocities.

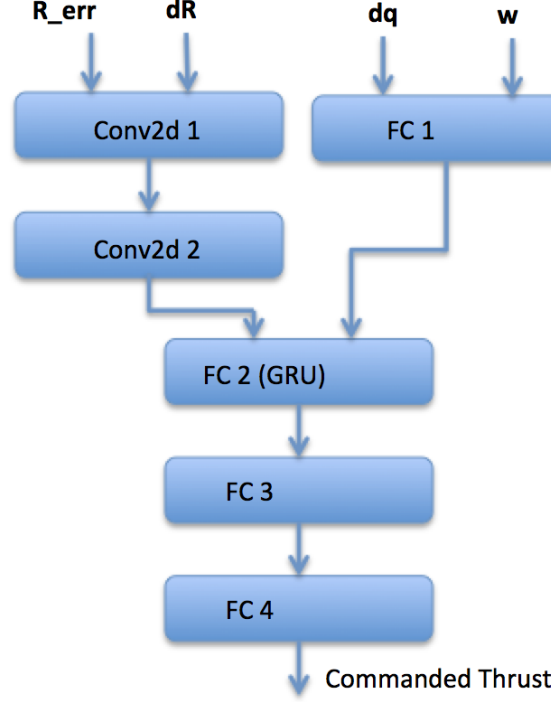


Fig. 4 Policy Network

Table 5 Hyperparameter Settings

α	β	γ	η	ζ	κ
-0.02	-0.01	-0.05	0.01	10	-50

A possible concept of operations would be for the spacecraft to slowly approach the asteroid using a navigation system that keeps the asteroid centered in a camera’s field of view, and then commence hovering when the mean range of the flash LIDAR elements is within some bounds. The initial conditions used for our experiments are given in Table 6. Note that the initial range is with respect to the asteroid’s surface given the line of sight to the asteroid center from the spacecraft’s initial position, i.e., a range of 100m implies an altitude of 100m with respect to the asteroid’s surface, regardless of the asteroid dimensions. Position θ and ϕ along with the initial range (plus the altitude offset) specify the spacecraft’s position in spherical coordinates in the asteroid centered reference frame. The spacecraft has a small uniformly distributed initial velocity. The spacecraft’s ideal initial attitude is such that the -Z body-frame axis is aligned with the line of sight to target. This ideal initial attitude is perturbed at the start of each episode such that the angle between the -Z body frame axis and line of sight to target varies uniformly as shown in Table 6. For lower altitude hovering positions where it is easier to insure most of the flash LIDAR beams give valid returns, the guidance algorithm can tolerate larger initial attitude errors.

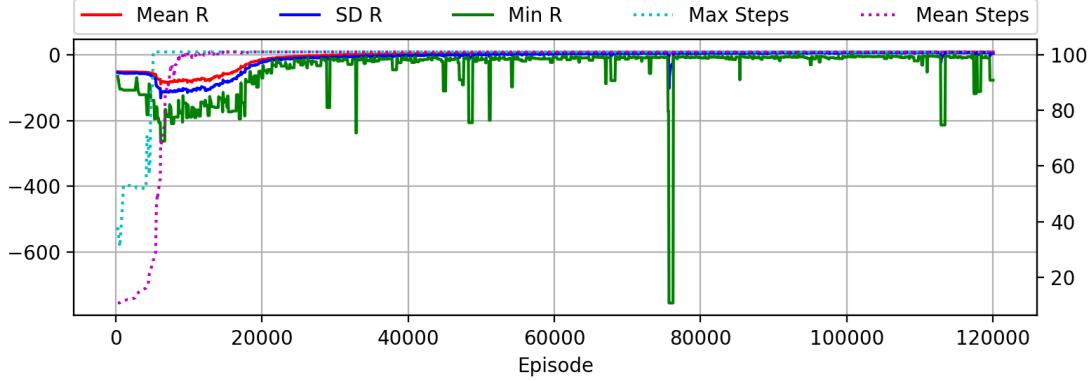
A. Optimization Results

We optimize using 30 episode rollouts and the initial conditions given in Table 6. To reduce computational requirements, we use an asteroid with only 320 facets for optimization. Each episode attempts to hover for 600s, but early termination is possible in the event of a constraint violation. For each episode, we randomly generate a new asteroid using parameters as given in Table 2. Fig. 5 plots reward statistics and Fig. 6 plots the terminal position error statistics, with statistics for both plots computed over rollout batch of 30 episodes. Note that during optimization there are rare catastrophic failures identifiable by the spikes in Figure 6. These are due to the fact that the exploration standard deviation was still around 0.20 (20% of maximum thrust) and slowly dropping when we terminated the optimization at 120,000 episodes. This exploration can occasionally result in the policy taking an action that results in catastrophic

Table 6 Initial Conditions

Parameter	min	max
Range (m)	200.0	700.0
Position θ (degrees)	0.0	90.0
Position ϕ (degrees)	$-\pi$	π
x component of Velocity (cm/s)	-10.0	10.0
y component of Velocity (cm/s)	-10.0	10.0
z component of Velocity (cm/s)	-10.0	10.0
Attitude Error (degrees)	0.0	11.0
x component of Rotational Velocity (mrad/s)	-5.0	5.0
y component of Rotational Velocity (mrad/s)	-5.0	5.0
z component of Rotational Velocity (mrad/s)	-5.0	5.0

failure, which is why we turn exploration off for the deployed policy. Note the initial rise in miss distance during the early phase of optimization. This is due to the agent focusing on satisfying the constraints that at least one element of the flash LIDAR sensor returns a valid reading and the maximum rotational velocity is not exceeded. Once the policy learns to satisfy the constraints, it focuses on minimizing the position error.

**Fig. 5 Optimization Rewards Learning Curves**

B. Policy Testing

For testing, we start with the same initial conditions and asteroid parameters used in optimization. Test results are given in Table 7, which are computed from 5000 simulated episodes. Note that the rotational velocity row in Table 7 gives the rotational velocity vector element with the worst performance. The "Good Hover 1" row gives the percentage of episodes where the terminal position error was less than 2m, terminal speed less than 10cm/s, and all elements of the terminal rotational velocity less than 0.025 rad/s. The "Good Hover 2" row has the same terminal speed and rotational velocity constraints, but only requires the terminal position error to be less than 5m. We did not achieve good terminal performance 100% of the time, as the terminal position error occasionally exceeded our requirements. Figure 7 illustrates the intersection of LIDAR beams with the asteroid for a typical initial condition, with misses shown as red beams. A sample trajectory is shown in Figure 8, where the position error subplot plots the deviation from the spacecraft's initial position. The "Estimated Value" subplot plots the value function's estimate of the value of the current state during the trajectory. Although the value function is not deployed with the policy, we thought this plot would be of interest. Note that when the environmental dynamics are such that maximum thrust is not required, the policy fires only a single thruster on a given side of the spacecraft, resulting in a 1N thrust. This saves fuel at the expense of inducing rotation, which is compensated for by firing the opposing thruster on the opposite side at some future time.

To illustrate the ability of the policy to generalize to novel initial conditions and asteroid characteristics, we re-ran testing using the cases tabulated in Table 8. In each case, performance was similar to that shown in Table 7, with the

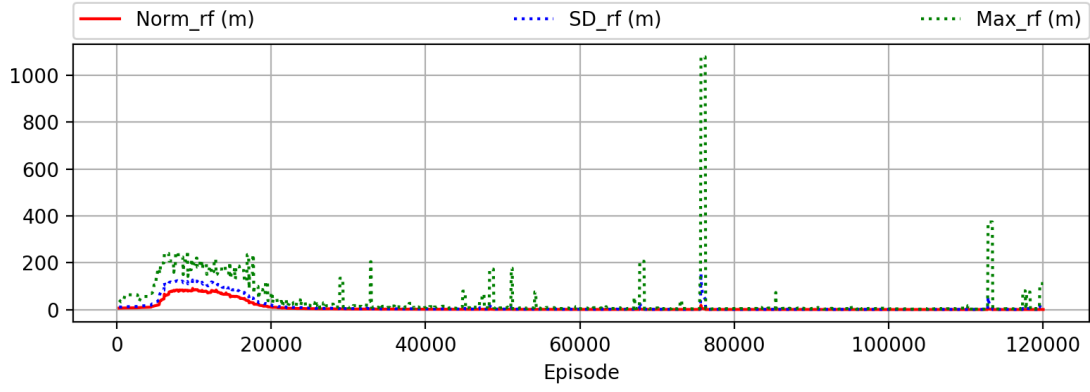


Fig. 6 Optimization Terminal Position Error Learning Curves

exception of increased fuel consumption for the extended hovering duration test.

Table 7 Performance

Parameter	Mean	Std	Max
Terminal Position (m)	0.554	0.362	3.331
Terminal Velocity (cm/s)	1.2	0.5	3.5
Rotational Velocity (mrad/s)	0.1	5.2	16.8
Good Hover 1 (%)	99.39	N/A	N/A
Good Hover 1 (%)	100.00	N/A	N/A
Fuel (kg)	0.61	0.09	0.92

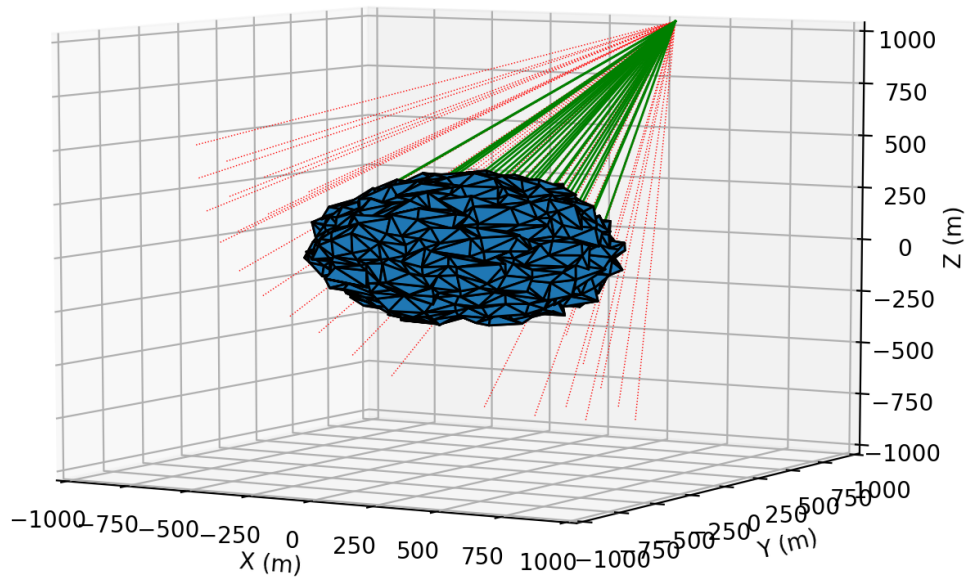


Fig. 7 Sample Initial LIDAR beam Intersections

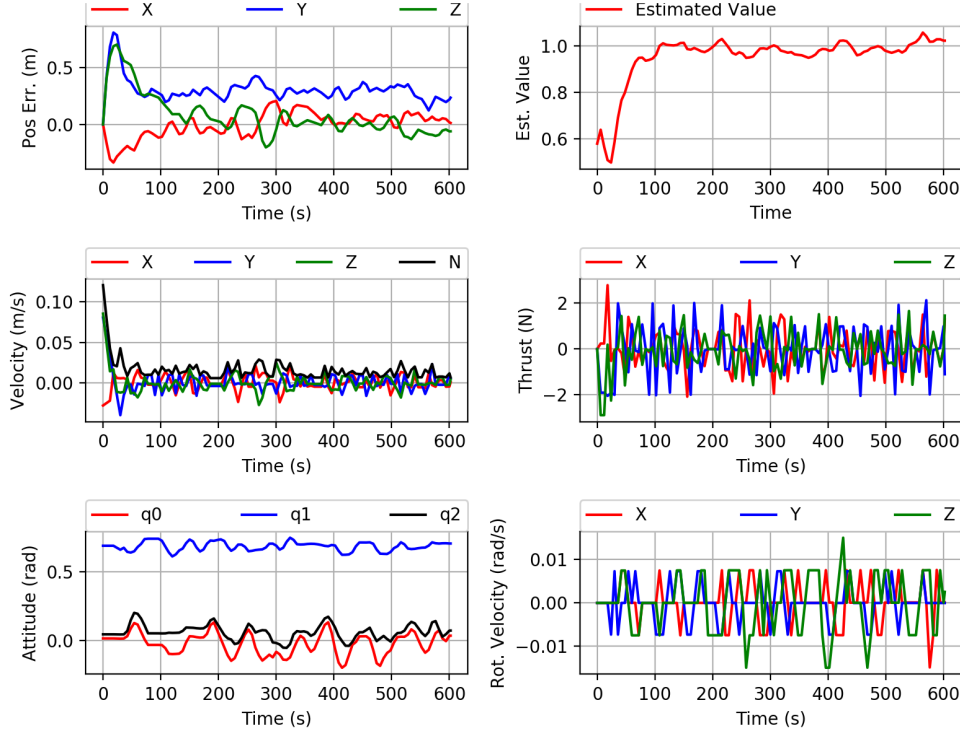


Fig. 8 Sample trajectory

Table 8 Generalization Cases

Case	Description
Extended Altitude Range	Initial altitude range increased to (10m, 700m)
Asteroid Facets	Number of facets on each randomly generated asteroid shape model increased from 320 to 1280
Asteroid Texture	We decreased the perturbation parameter for the randomly generated asteroid's vertices from 0.1 to 0.05
Hovering Duration	We increased hovering duration to 1200s

V. Conclusion

We formulated a particularly difficult problem that to our knowledge has not been solved: precision hovering in an asteroid's body-fixed frame without a shape model or navigation aids, and without knowledge of the asteroid's environmental dynamics. To solve this problem We created a high fidelity 6-DOF simulator that synthesized asteroid models with randomized parameters. where the asteroid is modeled as a uniform density ellipsoid that in general is not rotating about a principal axis, resulting in time varying dynamics. We then optimized an adaptive policy that mapped flash LIDAR sensor measurements directly to actuator commands. The policy was optimized using reinforcement meta-learning, where the policy and value function networks each contained a recurrent hidden layer, and with the policy network using a convolutional front-end. During optimization, the agent was confronted with a new randomly generated asteroid, with randomized shape, density, rotational speed, and nutation angle. We then demonstrated that

the optimized policy generalized to novel hovering altitudes, hovering duration, and asteroid shapes and textures. We expect that the ability to hover in the body-fixed frame immediately upon arrival at an asteroid will simplify shape model generation and other aspects of mission planning.

References

- [1] Schutz, B., Tapley, B., and Born, G. H., *Statistical orbit determination*, Elsevier, 2004.
- [2] Lara, M., and Scheeres, D. J., “Stability bounds for three-dimensional motion close to asteroids,” *The Journal of the astronomical sciences*, Vol. 50, No. 4, 2002, pp. 389–409.
- [3] Broschart, S. B., and Scheeres, D. J., “Control of hovering spacecraft near small bodies: application to asteroid 25143 Itokawa,” *Journal of Guidance, Control, and Dynamics*, Vol. 28, No. 2, 2005, pp. 343–354.
- [4] Sawai, S., Scheeres, D., and Broschart, S., “Control of hovering spacecraft using altimetry,” *Journal of Guidance, Control, and Dynamics*, Vol. 25, No. 4, 2002, pp. 786–795.
- [5] Furfaro, R., “Hovering in asteroid dynamical environments using higher-order sliding control,” *Journal of Guidance, Control, and Dynamics*, Vol. 38, No. 2, 2014, pp. 263–279.
- [6] Gaudet, B., and Furfaro, R., “Real-time state estimation for asteroid close-proximity operations via lidar altimetry and a particle filter,” *2013 AAS/AIAA Astrodynamics Specialist Conference, Astrodynamics 2013*, Univelt Inc., 2014.
- [7] Lee, D., Sanyal, A. K., Butcher, E. A., and Scheeres, D. J., “Almost global asymptotic tracking control for spacecraft body-fixed hovering over an asteroid,” *Aerospace Science and Technology*, Vol. 38, 2014, pp. 105–115.
- [8] Gaudet, B., and Furfaro, R., “Robust spacecraft hovering near small bodies in environments with unknown dynamics using reinforcement learning,” *AIAA/AAS Astrodynamics Specialist Conference*, 2012, p. 5072.
- [9] Mishra, N., Rohaninejad, M., Chen, X., and Abbeel, P., “A simple neural attentive meta-learner,” 2018.
- [10] Frans, K., Ho, J., Chen, X., Abbeel, P., and Schulman, J., “Meta learning shared hierarchies,” *arXiv preprint arXiv:1710.09767*, 2017.
- [11] Wang, J. X., Kurth-Nelson, Z., Tirumala, D., Soyer, H., Leibo, J. Z., Munos, R., Blundell, C., Kumaran, D., and Botvinick, M., “Learning to reinforcement learn,” *arXiv preprint arXiv:1611.05763*, 2016.
- [12] Gaudet, B., and Linares, R., “Adaptive Guidance with Reinforcement Meta-Learning,” *arXiv preprint arXiv:1901.04473*, 2019.
- [13] Gaudet, B., Linares, R., and Furfaro, R., “Seeker based Adaptive Guidance via Reinforcement Meta-Learning Applied to Asteroid Close Proximity Operations,” *arXiv preprint arXiv:1907.06098*, 2019.
- [14] Gaudet, B., Furfaro, R., and Linares, R., “A Guidance Law for Terminal Phase Exo-Atmospheric Interception Against a Maneuvering Target using Angle-Only Measurements Optimized using Reinforcement Meta-Learning,” *arXiv preprint arXiv:1906.02113*, 2019.
- [15] Scheeres, D. J., *Orbital motion in strongly perturbed environments: applications to asteroid, comet and planetary satellite orbiters*, Springer, 2016.
- [16] Möller, T., and Trumbore, B., “Fast, minimum storage ray/triangle intersection,” *ACM SIGGRAPH 2005 Courses*, ACM, 2005, p. 7.
- [17] Finn, C., Abbeel, P., and Levine, S., “Model-agnostic meta-learning for fast adaptation of deep networks,” *arXiv preprint arXiv:1703.03400*, 2017.
- [18] Gaudet, B., Linares, R., and Furfaro, R., “Deep Reinforcement Learning for Six Degree-of-Freedom Planetary Powered Descent and Landing,” *arXiv preprint arXiv:1810.08719*, 2018.
- [19] Schulman, J., Wolski, F., Dhariwal, P., Radford, A., and Klimov, O., “Proximal policy optimization algorithms,” *arXiv preprint arXiv:1707.06347*, 2017.
- [20] Schulman, J., Levine, S., Abbeel, P., Jordan, M., and Moritz, P., “Trust region policy optimization,” *International Conference on Machine Learning*, 2015, pp. 1889–1897.

- [21] Chung, J., Gulcehre, C., Cho, K., and Bengio, Y., “Gated feedback recurrent neural networks,” *International Conference on Machine Learning*, 2015, pp. 2067–2075.
- [22] Springenberg, J. T., Dosovitskiy, A., Brox, T., and Riedmiller, M., “Striving for simplicity: The all convolutional net,” *arXiv preprint arXiv:1412.6806*, 2014.